Chemical Engineering Journal 510 (2025) 161682

Contents lists available at ScienceDirect

Chemical Engineering Journal

journal homepage: www.elsevier.com/locate/cej

La-Ni-H metal hydride system aging effects identification

Yuanyuan Shang [a,*], Ting Chen [b], Fahim Karimi [a], Thi Thu Le [a], Jürgen Markmann [c,d], Jan Peter Embs [e], Benjamin Klusemann [b,f], Thomas Klassen [a,c,g], Claudio Pistidda [a,*]

[a] Department of Materials Design, Institute of Hydrogen Technology, Helmholtz-Zentrum hereon GmbH, 21502 Geesthacht, Germany
[b] Department of Solid State Materials Processing, Institute of Material and Process Design, Helmholtz-Zentrum hereon GmbH, 21502 Geesthacht, Germany
[c] Department of Hybrid Materials Systems, Institute of Hydrogen Technology, Helmholtz-Zentrum hereon GmbH, 21502 Geesthacht, Germany
[d] Institute of Materials Physics and Technology, Hamburg University of Technology, 21073 Hamburg, Germany
[e] PSI Center for Neutron and Muon Sciences, 5232 Villigen PSI, Switzerland
[f] Institute for Production Technology and Systems, Leuphana University Lüneburg 21335 Lüneburg, Germany
[g] Helmut Schmidt University, Holstenhofweg 85, 22043 Hamburg, Germany

ARTICLE INFO

Keywords:
Metal hydride
Aging effect
Hydrogen storage

ABSTRACT

One of the most commonly used materials for sorption compression in space applications is based on the La-Ni-H system. The degradation of the material properties and, therefore, the system lifetime is of great importance for the final success of a potential space mission. Considering that satellites and other equipment that have to operate in space are expected to be fully functional for more than 10 years, in this work, an accelerated aging method is designed and carried out to predict the La-Ni-H system properties after 12 years under specific operating conditions. For this test, several specimens of fully hydrogenated $LaNi_5$ are exposed to specific hydrogen pressures (i.e., 20, 35, 58 and 96 bar) at different temperatures (i.e., 50, 90, 130 and 160 °C) for a duration of 90 days. Sievert's type apparatus, synchrotron radiation powder X-ray diffraction (SR-PXD), quasi-elastic neutron scattering (QENS), scanning electron microscopy (SEM), and small-angle X-ray scattering (SAXS) methods are used to investigate the material aging and its impact on the material chemical and microstructural properties.

1. Introduction

Many highly sensitive instruments designed for space applications, e.g., infrared, gamma-ray and X-ray detectors, require constant cryogenic operating temperatures. While stored cryogens and passive cryoradiators have both been used for cryogenic cooling on numerous space missions, the ultimate goal of scientists and mission planners has always been to develop refrigerators capable of reaching relatively low cryogen temperatures (much lower than what passive radiators can achieve) and having a lifespan of several years [1]. In this regard, cryogenic coolers (cryocoolers) are essential for achieving accurate cryogenic temperature control in space [2,3]. However, the mechanical compressors that drive the first cryocoolers have moving parts and produce vibration, which significantly hinders their practical applications when combined with highly sensitive equipment.

With features like low vibration, no electromagnetic interference, high reliability, and extended operating life, sorption compressors based on the Joule–Thomson (J–T) effect are becoming viable solutions for space applications [4]. The sorbents used for the sorption compressors can be divided into two types based on the working mechanism, i.e., physical and chemical. Metal-based systems with a particular affinity for hydrogen can serve as sorbent materials in sorption compressors, regulating temperatures by varying hydrogen pressures and flow rates [5,6]. Moreover, metal hydride sorbents are non-corrosive, non-toxic, and easy to handle, rendering them appealing for such purposes. $LaNi_5$, a well-studied low-temperature metal hydride [7], has been already utilized in these space sorption compressors for the European Space Agency (ESA) Planck Mission [3,8].

In light of the fact that satellites and other space-related equipment must run flawlessly for often more than ten years, an accelerated aging method was developed in this work to forecast the La-Ni-H system features after twelve years of operation. The as received and aged samples' hydrogen storage properties were investigated by Sievert's type apparatus and microstructures were characterized by synchrotron radiation

---

[*] Corresponding authors at: Department of Materials Design, Institute of Hydrogen Technology, Helmholtz-Zentrum hereon GmbH, 21502 Geesthacht, Germany (Y. Shang).

E-mail addresses: yuanyuan.shang@hereon.de (Y. Shang), claudio.pistidda@hereon.de (C. Pistidda).

https://doi.org/10.1016/j.cej.2025.161682
Received 16 December 2024; Received in revised form 21 February 2025; Accepted 16 March 2025

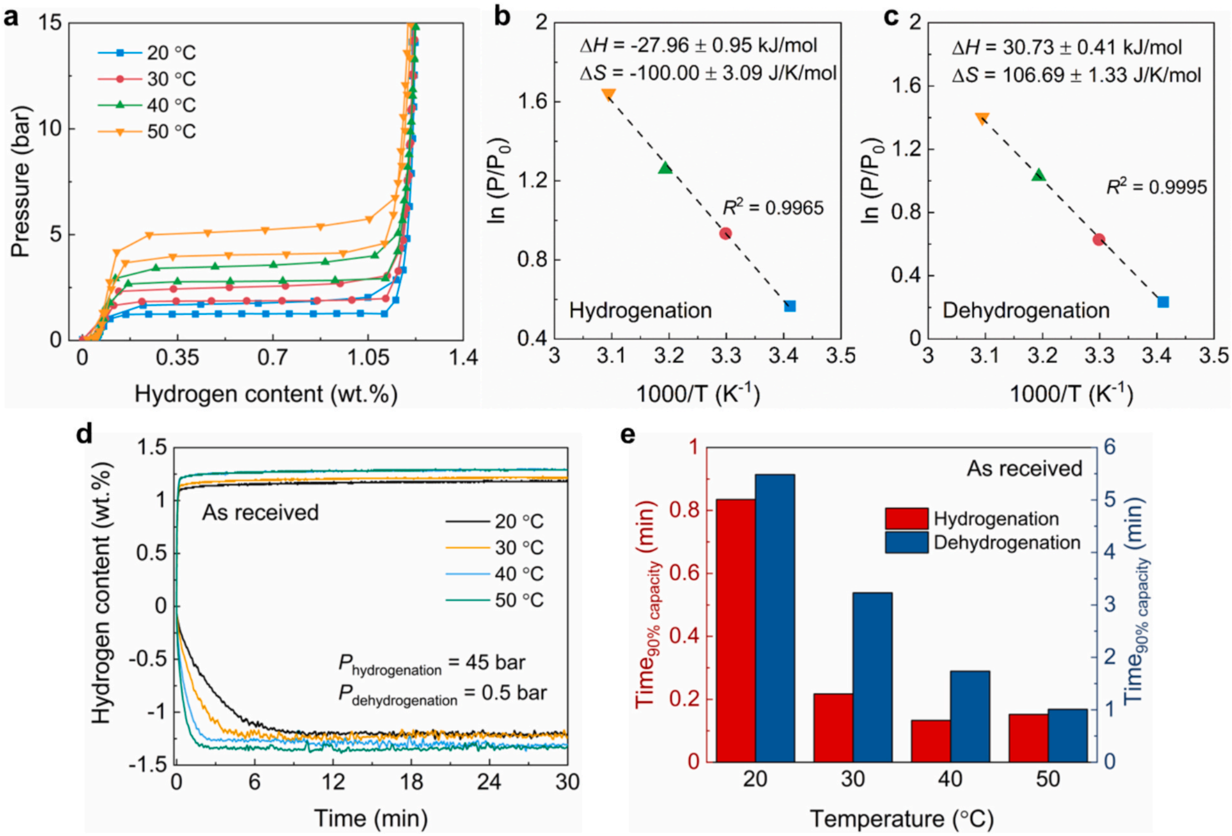

Fig. 1. Hydrogen storage properties of the as received LaNi$_5$ sample. a Pressure composition isotherm (PCI) curves of the as received material at 20, 30, 40 and 50 °C. **b-c** The corresponding ΔH and ΔS for hydrogenation and dehydrogenation, respectively. **d-e** Hydrogenation and dehydrogenation kinetic curves of the as received material at 20, 30, 40 and 50 °C, respectively. The hydrogenation pressures are around 45 bar of hydrogen, whilst the dehydrogenation pressures are around 0.5 bar of hydrogen.

powder X-ray diffraction (SR-PXD), quasi-elastic neutron scattering (QENS), small-angle X-ray scattering (SAXS), and scanning electron microscopy (SEM) methods.

2. Experimental methods

The investigated material in this study was extracted from a rechargeable hydrogen container model BL-30, purchased from Hydrogen Components, Inc. The extracted material consisted of LaNi$_5$ plus ca. 5 wt% of Teflon^{TM} i.e., polytetrafluoroethylene (PTFE), which is referred to as LaNi$_5$ in the following. The opening of the tank and the powder material handling were carried out in an Ar-filled glovebox (O_2 and H_2O levels < 1 ppm).

To characterize the materials' hydrogen storage properties, the samples were loaded into a PCT-Pro Setaram & Hy-Energy manometric Sievert-type apparatus and evacuated for 30 min at room temperature. Then the samples were exposed to helium for volume calibration (pressure in the range of 3 – 5 bar). The overall procedure lasted about 15 min. Pressure composition isotherm (PCI) measurements were performed at different temperatures, i.e., 20, 30, 40, and 50 °C. The temperature of the sample holder was controlled by a water bath (CORIO CD-601F, Julabo GmbH). The variations of reaction enthalpy (ΔH) and entropy (ΔS) for hydrogenation/dehydrogenation were obtained utilizing the van't Hoff equation (**Eq.** (1)) and previously acquired PCI measurements:

$$\ln\frac{P_{eq}}{P_0} = \frac{\Delta H}{RT} - \frac{\Delta S}{R} \tag{1}$$

where P_0 is the standard pressure, P_{eq} is the equilibrium pressure, R is the universal gas constant and T represents the sample temperature. The kinetic properties of the as received sample were investigated by using a PCT-Pro Setaram and a Hy-Energy manometric Sievert-type apparatus. The measurements were carried out at 20, 30, 40 and 50 °C, while the hydrogen pressures applied to the specimens for the hydrogenation and the dehydrogenation measurements were 45 and 0.5 – 2 bar, respectively.

An accelerated calendar aging method [9] was used to predict the aging behavior of the material, assuming that the aging follows an Arrhenius behavior:

$$\alpha = A \bullet exp\left(\frac{-E_a}{RT}\right) \tag{2}$$

where A is a fitting parameter based on the relationship of the properties and the temperatures and E_a is the activation energy of the reaction that happens at temperature T. Note that α represents different factors that are related to the material properties, i.e. change of capacity and equilibrium pressure. The original batch of LaNi$_5$ was divided into several smaller batches and subjected to 20, 35, 58 and 96 bar of hydrogen pressure for 90 days at temperatures of 50, 90, 130 and 160 °C, respectively. The samples were loaded into stainless sample holders and were kept at the above-mentioned temperatures by using oil baths and ceramic ovens. Aluminum foils were employed to cover the conical flasks to mitigate heat and oil losses.

Microstructural investigations using synchrotron radiation powder X-ray diffraction (SR-PXD) were conducted at beamline P02.1, PETRA III of DESY in Hamburg, Germany. A Varex 4343CT detector was used, and the wavelength was set at 0.2074 Å. A LaB$_6$ standard from NIST was used to calibrate the sample-to-detector distance (SDD). The samples were loaded into the glass capillaries and sealed with glue inside an Ar-

Table 1
Thermodynamic properties obtained from PCI curves for the as received, 50, 90, 130 and 160 °C aged $LaNi_5$.

Sample	Temperature (°C)	Hydrogenation			Dehydrogenation		
		Equilibrium pressure (bar)	Enthalpy (kJ·mol^{-1})	Entropy (J·mol^{-1}K^{-1})	Equilibrium pressure (bar)	Enthalpy (kJ·mol^{-1})	Entropy (J·mol^{-1}K^{-1})
As received	20	1.76	−27.96 ± 0.95	−100.00 ± 3.09	1.26	30.73 ± 0.41	106.69 ± 1.33
	30	2.54			1.87		
	40	3.52			2.80		
	50	5.17			4.06		
50 °C aged	20	1.77	−29.95 ± 0.13	−106.89 ± 0.42	1.10	33.73 ± 0.81	116.03 ± 2.63
	30	2.64			1.83		
	45	4.66			3.32		
	55	6.54			4.88		
90 °C aged	20	1.50	–32.99 ± 0.92	−115.81 ± 2.96	1.14	32.77 ± 0.12	112.85 ± 0.37
	30	2.31			1.77		
	45	4.15			3.26		
	55	6.44			4.79		
130 °C aged	20	1.45	−29.68 ± 2.58	−103.78 ± 8.33	0.92	34.44 ± 0.31	116.78 ± 1.01
	30	1.87			1.45		
	45	3.40			2.77		
	55	5.25			4.18		
160 °C aged	20	0.68	−21.50 ± 2.29	−69.60 ± 7.38	0.42	29.40 ± 0.36	92.98 ± 1.18
	30	0.78			0.61		
	45	1.28			1.06		
	55	1.67			1.51		

filled glovebox (O_2 and H_2O levels < 1 ppm). FIT2D software was used to convert the recorded 2D images into numerical data [10].

Quasi-elastic neutron scattering (QENS) measurements were conducted with cold neutrons using the time-of-flight neutron spectrometer (FOCUS) located at the continuous spallation source SINQ at the Paul Scherrer Institute (Villigen, Switzerland). The incident neutron wavelength was 4.4 Å, and the elastic scattering energy resolution, $\delta(E)$, was 0.223 meV (full width at half maximum, FWHM), corresponding to an observable time $\tau \approx 2\hbar/\text{FWHM}$ of 5.9 ps. The samples were loaded into sealed aluminum cylinders (6-mm diameter) inside the Ar-continuously filled glovebox. The spectra were recorded in a range of scattering vectors from $Q = 0.3$ to 2.5 Å^{-1}. Data reduction was carried out using the DAVE software (data analysis and visualization environment). The acquired QENS spectra were analyzed using the curve fitting utility PAN included in DAVE. The measured total incoherent scattering function $S(Q,\omega)$ (**Eq. (3)**) can be expressed as a convolution of an elastic scattering described by the delta function $\delta(\omega)$ and a quasi-elastic contribution described by the Lorentzian function $L(Q,\omega)$, with a flat background (bg) to account for fast motions and the resolution function of the instrument $R(Q,\omega)$ determined using a vanadium standard:

$$S(Q,\omega) = R(Q,\omega) \otimes [I_{el}\delta(\omega) + I_{qe}\, L(Q,\omega)] + bg \quad (3).$$

where I_{el} and I_{qe} are the elastic and integrated quasi-elastic scattering intensities, respectively.

The morphologies of the materials were revealed by using a field-emission scanning electron microscope (FEI Quanta 650 SEM) in both secondary electron (SE) and backscattered electron (BSE) modes. The preparation of the sample was handled in an Ar-filled glovebox with values of O_2 and $H_2O < 1$ ppm. For each sample, 200 particles were selected in order to get the average particle size and analyze the particle size distribution. Energy dispersive X-ray spectroscopy (EDS) with an EDAX system equipped in the SEM was used to analyze the elemental compositions of the targeted areas for the samples.

The microstructural features of the investigated samples were further investigated using a laboratory SAXS instrument (Xenocs Xeuss 3.0 system). The instrument was equipped with a Dectris Pilatus3 R 300 K detector and microfocus tubes with Cu and Mo anodes as sources operated at 50 kV and 0.6 mA (Cu) and 1.0 mA (Mo). In this investigation, the K_α radiation line (0.71 Å) of the Molybdenum source was applied to acquire the SAXS data. All SAXS samples were prepared inside a glovebox with a continuously running purified Argon flow. The powdered samples were placed inside a circular hole of an aluminum holder and sealed on both sides with Kapton tape to avoid any change in the oxidation state of the samples by the transfer to the SAXS instrument and during the measurements. Furthermore, all measurements were conducted under dynamic vacuum to prevent possible oxidation state of the samples and to avoid any air scattering during the SAXS measurements. In addition, the primary beam and an empty holder only with Kapton tape were measured to determine the transmission values of the samples. For all SAXS measurements, the area of illumination on the samples was set to roughly 500 × 500 μm^2. The measurements were carried out at two SDD ($d_{short} = 900$ mm and $d_{long} = 1800$ mm) in order to cover the desired q-range, with an exposure time of 240 s and 3000 s, respectively. The aforementioned quantity q describes the scattering vector of the incident beam, which is given by: $q = (4\pi/\lambda)sin\theta$, where 2θ refers to the scattering angle of the elastically scattered photons and λ is the corresponding monochromatic wavelength. All the fittings were done by SASfit software [11].

3. Results and discussion

3.1. Properties of the as received material

Firstly, the thermodynamic and kinetic properties of the as received $LaNi_5$ were investigated. As the material readily absorbs hydrogen, no activation process was carried out prior to starting these investigations. Fig. 1a-c illustrates the PCI curves and the corresponding calculations of the ΔH and ΔS for both hydrogenation and dehydrogenation processes. The overall capacity of the as received material is around 1.27 wt%. The hydrogenation and dehydrogenation plateau pressures measured at half of the plateau length, for the PCI measurement carried out at 20 °C, are 1.76 and 1.26 bar, respectively. At 30 °C, the plateau pressures for hydrogenation and dehydrogenation are 2.54 and 1.87 bar, respectively. At 40 °C, the values are 3.52 and 2.80 bar, respectively. Whereas the hydrogenation and dehydrogenation plateau pressures at 50 °C are 5.17 and 4.06 bar, respectively. The plateau pressure values of this specimen and for the aged ones are reported in Table 1. By using the plateau pressure values measured at 20, 30, 40 and 50 °C, for the hydrogenation process, an enthalpy of reaction (ΔH) equals to -27.96 ± 0.95 kJ·mol^{-1} and an entropy variation (ΔS) equals to -100.00 ± 3.09 J·mol^{-1}K^{-1} were obtained. Whereas for the dehydrogenation process, the obtained

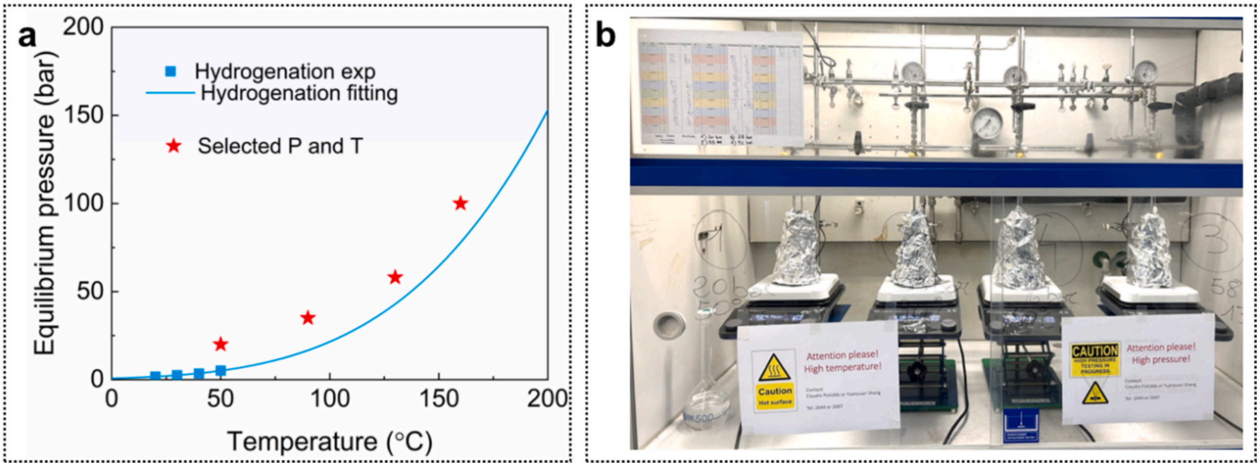

Fig. 2. Setup of the accelerated aging measurements. **a** Equilibrium pressure–temperature curves of the investigated $LaNi_5$ materials and selected temperatures and corresponding pressures for aging measurements. **b** Setup for the accelerated aging measurements for 90 days.

values were $\Delta H = 30.73 \pm 0.41$ kJ·mol^{-1} and $\Delta S = 106.69 \pm 1.33$ J·mol^{-1}K^{-1}. The kinetic properties of the materials at 20, 30, 40 and 50 °C are reported in Fig. 1d. From these measurements, a hydrogen storage capacity of the as received material of around 1.25 wt% is observed. For all the investigated temperatures, the hydrogenation process is faster than the dehydrogenation process. For all temperatures tested, the hydrogenation process takes less than 1 min to reach 90 % of the entire hydrogenation capacity (Fig. 1e). Under all temperatures investigated, the dehydrogenation process takes less than 6 min; however, as the temperature decreases, the reaction rate steadily decreases.

3.2. Accelerated aging tests

To identify potential aging phenomena, accelerated aging tests were carried out. The applied temperatures and hydrogen pressures for the accelerated aging test were selected based on the equilibrium pressure–temperature curves of the as received $LaNi_5$ and based on a hypothetical practical operating temperature of 50 °C in a hydrogenated state. To know the conditions of pressure and temperature where the material is in a fully hydrogenated state, a series of PCI measurements were carried out, see Fig. 1a. From the obtained data (Table 1), an equilibrium pressure curve was extrapolated for temperatures up to 200 °C, see Fig. 2a. Based on this, the temperatures chosen for aging the as received material were 50, 90, 130 and 160 °C at hydrogen pressures of 20, 35, 58 and 96 bar, respectively. The temperatures for the accelerated aging measurements were chosen arbitrarily in a way that significant information on the material's aging in a reasonable time frame could be acquired, taking into account the instrumental limitations of the setup (e.g., 100 bar maximum hydrogen pressure applicable to prevent the metal hydride from decomposing). The tests were performed on the setup shown in Fig. 2b. The specimens were kept under constant temperature and pressure conditions for 90 days.

Fig. 3a exhibits the PCI curves of the material aged at 50 °C for 90 days measured at 20, 30, 45 and 55 °C. After aging at 50 °C for 90 days, the measured hydrogen storage capacity is around 1.22 wt%, which is comparable to that of the as received material. As can be seen in Table 1, the PCI's curves measured at 20 and 30 °C show hydrogenation plateau pressures higher (0.01 to 0.1 bar) than those of the as received materials. However, for the dehydrogenation plateau pressures at 20 and 30 °C, the values are ca. 0.16 and 0.04 bar lower than those of the as received material. The hydrogenation and dehydrogenation plateau pressures at 45 °C are 4.66 and 3.32 bar, respectively. Whereas the hydrogenation and dehydrogenation plateau pressures at 55 °C are 6.54 and 4.88 bar, respectively. This indicates that after aging, the difference between hydrogenation and dehydrogenation, i.e. hysteresis, increases. Fig. 3b and c illustrate the van't Hoff plots and associated hydrogenation and dehydrogenation ΔH and ΔS values for $LaNi_5$ aged at 50 °C. For the hydrogenation process, $\Delta H = -29.95 \pm 0.13$ kJ·mol^{-1} and $\Delta S = -106.89 \pm 0.42$ J·mol^{-1}K^{-1} were determined, whereas for the dehydrogenation process, $\Delta H = 33.73 \pm 0.81$ kJ·mol^{-1}; $\Delta S = 116.03 \pm 2.63$ J·mol^{-1}K^{-1}were obtained. The values for the ΔH and ΔS are greatly different from the as received materials, indicating that the material's microstructure may be changed due to aging.

Similar to at 50 °C, Fig. 3d displays the PCI curves of the material aged at 90 °C for 90 days. The material has a hydrogen storage capability of around 1.2 wt%. Also in this case, the hydrogenation plateau pressures for the curves measured at 20 and 30 °C are 0.24 and 0.44 bar higher than the values of the as received $LaNi_5$. The dehydrogenation plateau pressures at 20 and 30 °C are 1.14 and 1.77 bar, respectively. The hydrogenation plateau pressures at 45 and 55 °C are 4.15 and 6.44 bar, respectively. The dehydrogenation plateau pressures at 45 and 55 °C are 3.26 and 4.79 bar, respectively, see Table 1. The corresponding ΔH and ΔS for hydrogenation and dehydrogenation are $\Delta H = –32.99 \pm 0.92$ kJ·mol^{-1} and $\Delta S = -115.81 \pm 2.96$ J·mol^{-1}K^{-1}and $\Delta H = 32.77 \pm 0.12$ kJ·mol^{-1} and $\Delta S = 112.85 \pm 0.37$ J·mol^{-1}K^{-1}, respectively (Fig. 3e and f). In this case too, the ΔH and ΔS values differ significantly from those of the materials received, although they are similar to the sample that was aged for 90 days at 50 °C (Fig. 3b-c).

The PCI curves of the material aged at 130 °C for 90 days at 20, 30, 45 and 55 °C in Fig. 3g demonstrate a material hydrogen storage capacity of 1.05 wt%, thus significantly lower than the previously investigated specimens. Additionally, for the curves measured at 20 and 30 °C, the average hydrogenation plateau pressures (1.45 bar at 20 °C and 1.87 bar at 30 °C) are close to that of the as received materials but the plateaus present significant slopes. Similar to previous aged samples, the dehydrogenation plateau pressures at 20 and 30 °C for the 130 °C aged sample are around 0.34 and 0.42 bar lower than the values for the as received material. The hydrogenation plateau pressures at 45 and 55 °C are 3.40 and 5.25 bar, respectively. The dehydrogenation plateau pressures at 45 and 55 °C are 2.77 and 4.18 bar, respectively, see Table 1. From the calculations in Fig. 3h and i, the following values of enthalpy and entropy variations for the hydrogenation and dehydrogenation processes were obtained, i.e., $\Delta H = -29.68 \pm 2.58$ kJ·mol^{-1} and $\Delta S = -103.78 \pm 8.33$ J·mol^{-1}K^{-1}, and $\Delta H = 34.44 \pm 0.31$ kJ·mol^{-1} and $\Delta S = 116.78 \pm 1.01$ J·mol^{-1}K^{-1}.

When aged at 160 °C for 90 days, the overall material hydrogen storage capacity significantly decreases to 0.68 wt%, whereas the plateau length is only 0.5 wt% (see Fig. 3j), and the plateaus are markedly sloppy. At a given temperature, PCI curves should show a flat plateau consequent to the continuous conversion between α phase (alloy

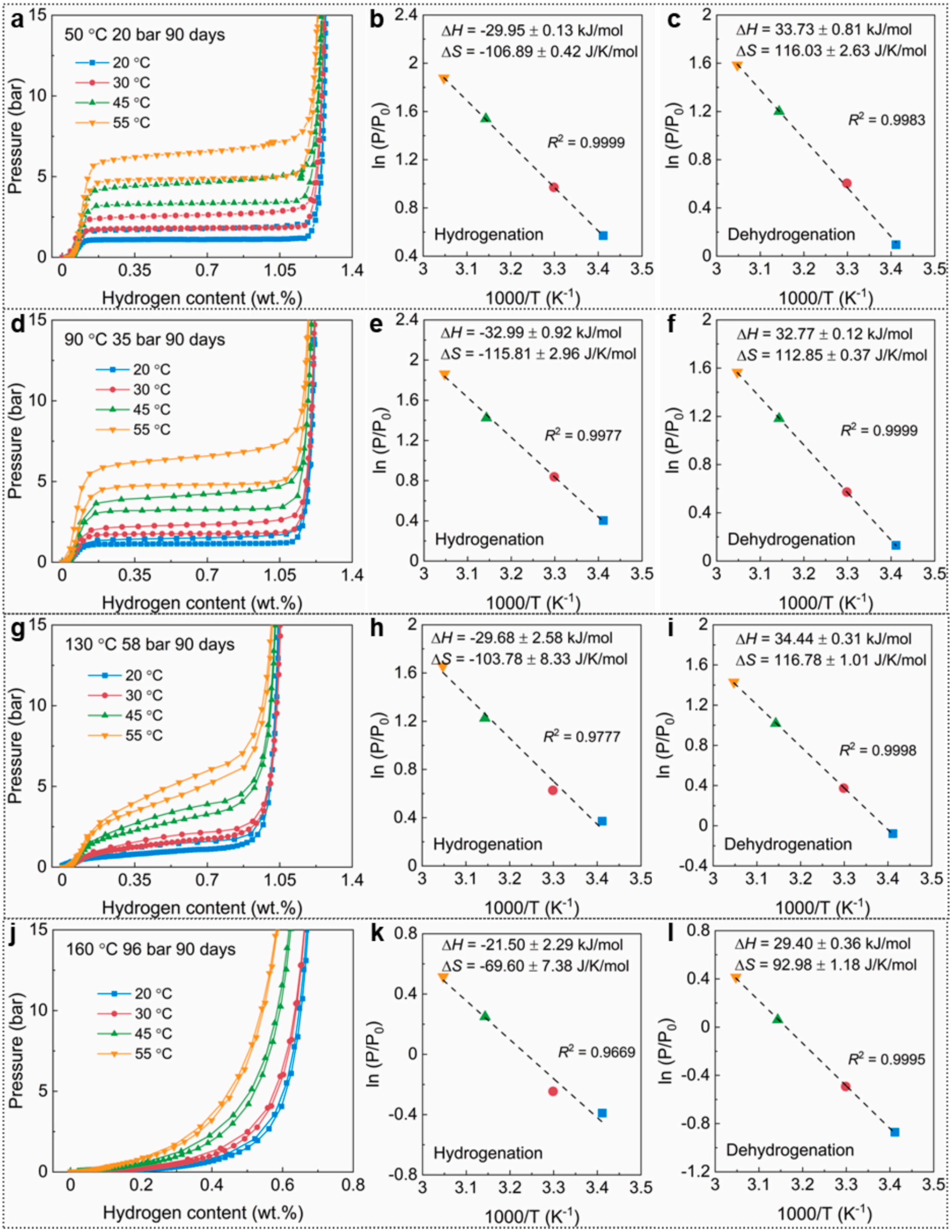

Fig. 3. Thermodynamic properties of the materials after accelerated aging tests. a PCI curves of the material aging at 50 °C for 90 days. **b, c** The corresponding Δ*H* and Δ*S* for hydrogenation and dehydrogenation of 50 °C aged $LaNi_5$, respectively. **d** PCI curves of the material aging at 90 °C for 90 days. **e, f** The corresponding Δ*H* and Δ*S* for hydrogenation and dehydrogenation of 90 °C aged $LaNi_5$, respectively. **g** PCI curves of the material aging at 130 °C for 90 days. **h, i** The corresponding Δ*H* and Δ*S* for hydrogenation and dehydrogenation of 130 °C aged $LaNi_5$, respectively. **j** The PCI curves of the material aging at 160 °C for 90 days. **k, l** The corresponding Δ*H* and Δ*S* for hydrogenation and dehydrogenation of 160 °C aged $LaNi_5$, respectively.

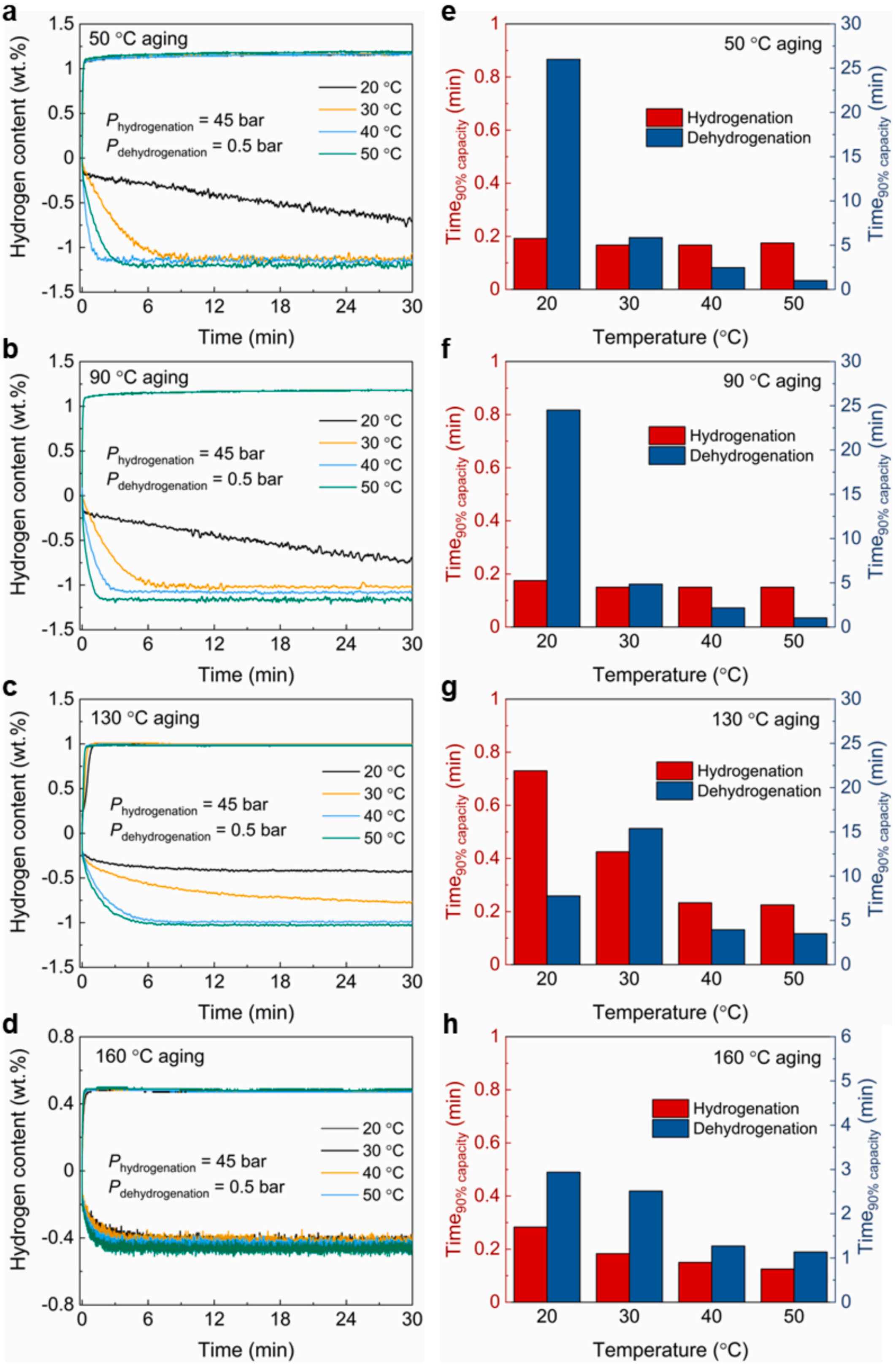

Fig. 4. Kinetic properties of the materials after accelerated aging tests. a-d Hydrogenation and dehydrogenation kinetic curves (at 20, 30, 40 and 50 °C) of the 50 °C, 90 °C, 130 °C and 160 °C aged materials, respectively. The hydrogenation pressures are around 45 bar of hydrogen, whilst the dehydrogenation pressures are around 0.5 bar of hydrogen. **e-h** The time needed to reach 90 % of the overall hydrogenation and dehydrogenation capacities for the 50 °C, 90 °C, 130 °C and 160 °C aged materials, respectively.

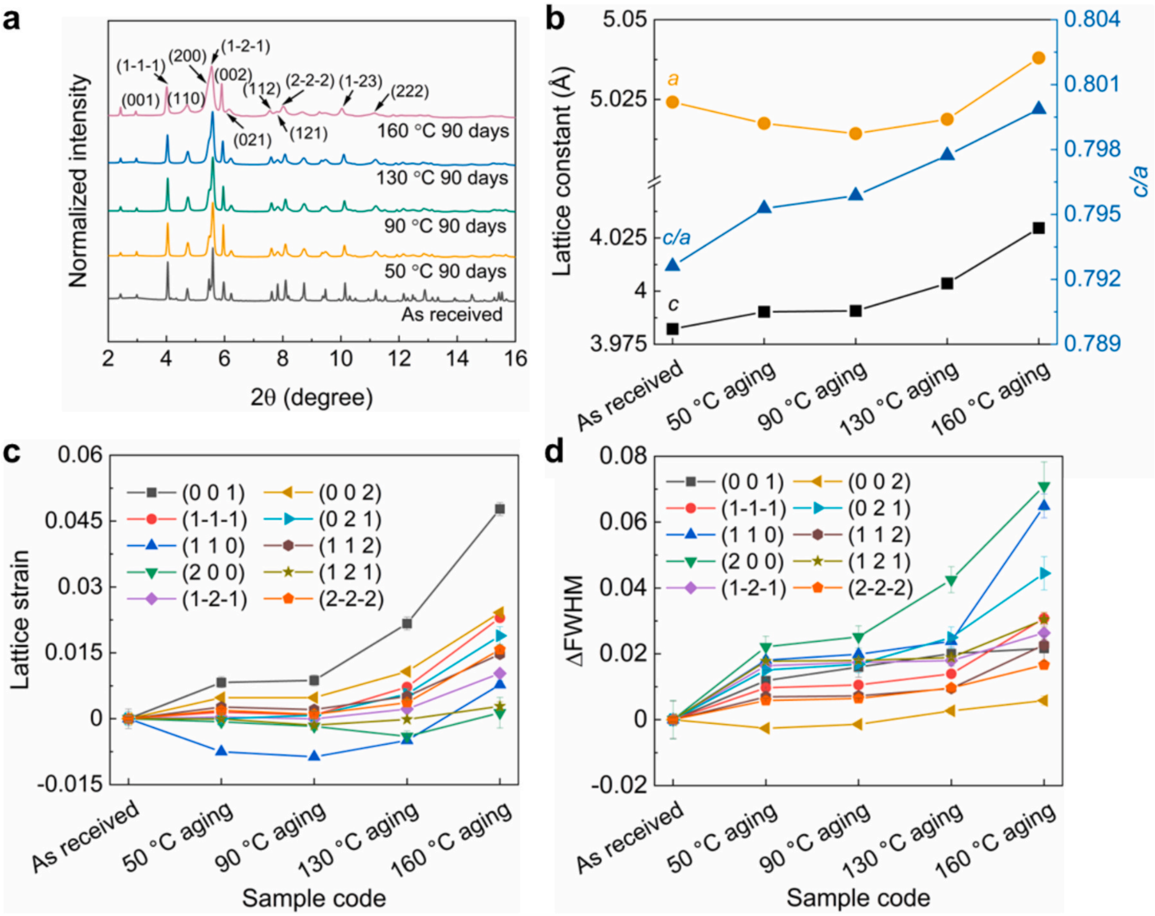

Fig. 5. Synchrotron radiation powder X-ray diffraction (SR-PXD) analyses of the as received and aged materials ($\lambda = 0.2074$ Å). a SR-PXD patterns of the sample as received and the samples aged at 50, 90, 130 and 160 °C for 90 days. **b** Lattice constants and *c* to *a* ratios of the sample as received and the samples aged at 50, 90, 130 and 160 °C for 90 days. **c** Lattice strains of some lattice planes for the sample as received and the samples aged at 50, 90, 130 and 160 °C for 90 days. **d** The change of full width at half maximum (FWHM) for the sample as received and the samples aged at 50, 90, 130 and 160 °C for 90 days.

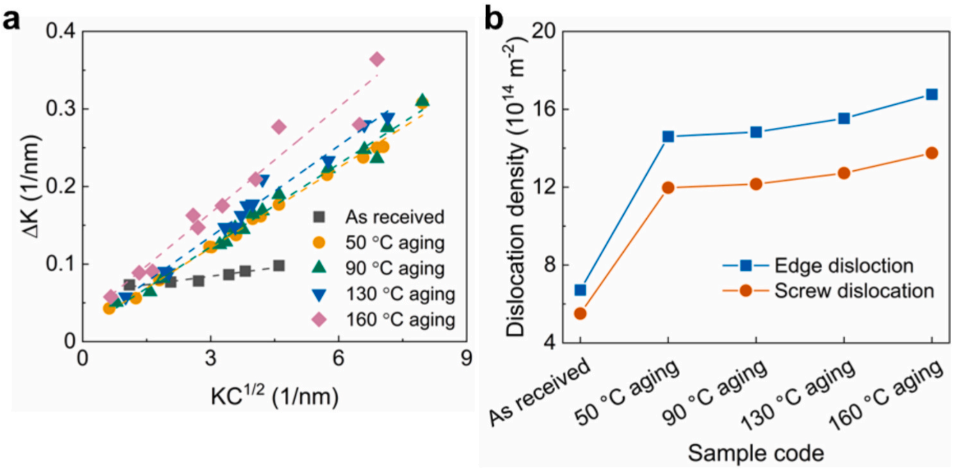

Fig. 6. Defects analyses from SR-PXD data ($\lambda = 0.2074$ Å) for the sample as received and the samples aged at 50, 90, 130 and 160 °C for 90 days. a Physical line broadening ΔK versus $KC^{1/2}$ by using the modified Williamson-Hall method. Where K is the peak position and C is the average contrast factor. **b** Dislocation densities of the sample as received and the samples aged at 50, 90, 130 and 160 °C for 90 days.

– hydrogen solid solution) and β phase (hydride phase), but metal hydrides often do not exhibit a perfectly flat plateau due to local chemical inhomogeneities. This is the case of the materials investigated in this work. In the case of the 160 °C aged sample, the PCI measurements do not show clear plateaus. To keep consistency with the other samples, the pressure values in the middle of the absorption curve were considered for determining the hydrogenation/dehydrogenation enthalpies and entropies. The identification of the material aging mechanism did not take the pressure values of 160 °C aged sample into account. The hydrogenation plateau pressures at 20 and 30 °C significantly decrease to

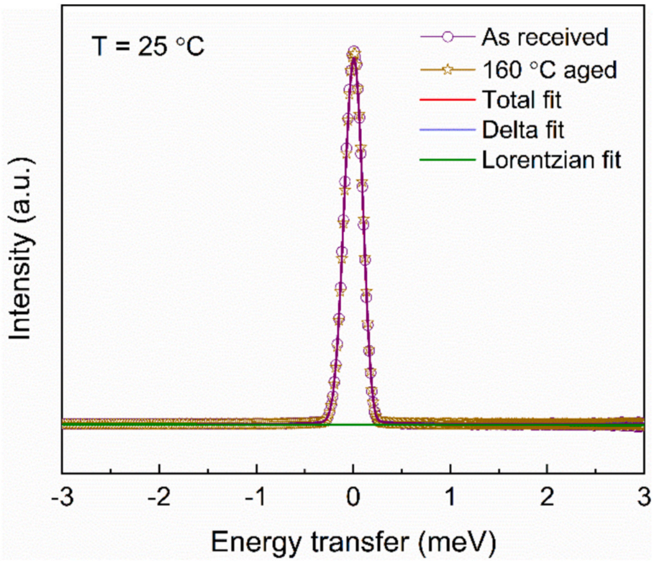

Fig. 7. Quasi-elastic neutron scattering spectrum of as received and 160 °C aged $LaNi_5$, measured at 25 °C using 4.4 Å incident neutron. The red line represents the fitting to the data with two components: Delta function (blue line) and Lorentzian profile (green line). (For interpretation of the references to colour in this figure legend, the reader is referred to the web version of this article.)

0.67 and 0.78 bar, respectively. Compared to the dehydrogenation plateau pressures for the as received $LaNi_5$, the values at 20 and 30 °C decrease to 0.42 and 0.61 bar, respectively. The hydrogenation plateau pressures at 45 and 55 °C are 1.28 and 1.67 bar, respectively. The dehydrogenation plateau pressures at 45 and 55 °C are 1.06 and 1.51 bar, respectively, see Table 1. The corresponding ΔH and ΔS for hydrogenation and dehydrogenation are shown in Fig. 3k and l, respectively. The absolute enthalpy and entropy values for both hydrogenation and dehydrogenation are smaller than those of the previously mentioned samples. For the hydrogenation process, $\Delta H = -21.50 \pm 2.29$ kJ·mol^{-1} and $\Delta S = -69.60 \pm 7.38$ J·mol^{-1}K^{-1}; For the dehydrogenation process, $\Delta H = 29.40 \pm 0.36$ kJ·mol^{-1} and $\Delta S = 92.98 \pm 1.18$ J·mol^{-1}K^{-1}. However, due to the fact that the obtained ΔH and ΔS for the 160 °C aged sample have large errors, they were not used for subsequent aging calculations.

The kinetic properties of the 50 °C aged material at 20, 30, 40 and 50 °C are shown in Fig. 4**a**. The overall capacity of the sample is about 1.18 wt%. The hydrogenation process can reach 90 % capacity within 1 min at all the investigated temperatures, see Fig. 4e. For the dehydrogenation process, it is worth noting that the dehydrogenation at 20 °C proceeds rather slowly, and only 0.70 wt% of hydrogen can be released within the timeframe of 30 min. When the dehydrogenation temperature increases, the time decreases to less than 6 min. Fig. 4b shows the results of hydrogenation and dehydrogenation at 20, 30, 40 and 50 °C for 90 °C aged $LaNi_5$, with an overall hydrogen capacity of about 1.18 wt %. Similar to the 50 °C aged sample, the hydrogenation process is relatively faster than the dehydrogenation process, completing 90 % of the reaction in less than 1 min. For the dehydrogenation process, only 0.75 wt% hydrogen can be released in 30 min at 20 °C. As the measuring temperature is increased, the kinetic rates increase, as illustrated in Fig. 4b and Fig. 4f. Under identical experimental conditions, the hydrogen concentration of the sample aged at 130 °C is 0.99 wt%, as illustrated in Fig. 4c. Note that there is a significant difference between the dehydrogenation kinetic properties at 20, 30 °C and other

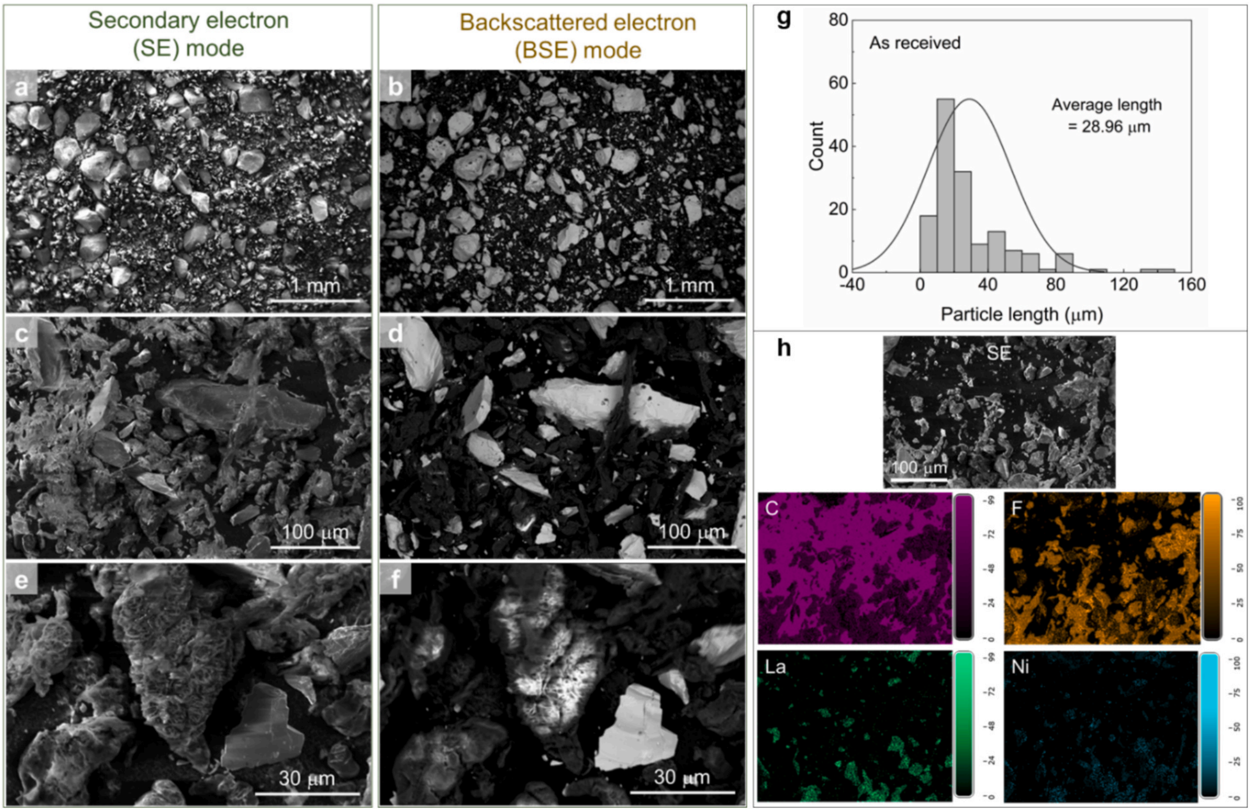

Fig. 8. Scanning electron microscope (SEM) results of the as received $LaNi_5$. a, c, e Secondary electron (SE) images of the as received material at different magnifications. **b, d, f** The corresponding backscattered electron (BSE) images of the as received material at different magnifications. **g** The particle size distribution obtained by SEM. **h** The SE image of the as received material and corresponding energy dispersive X-ray spectroscopy (EDS) mapping for the elements of C, F, La, and Ni, respectively.

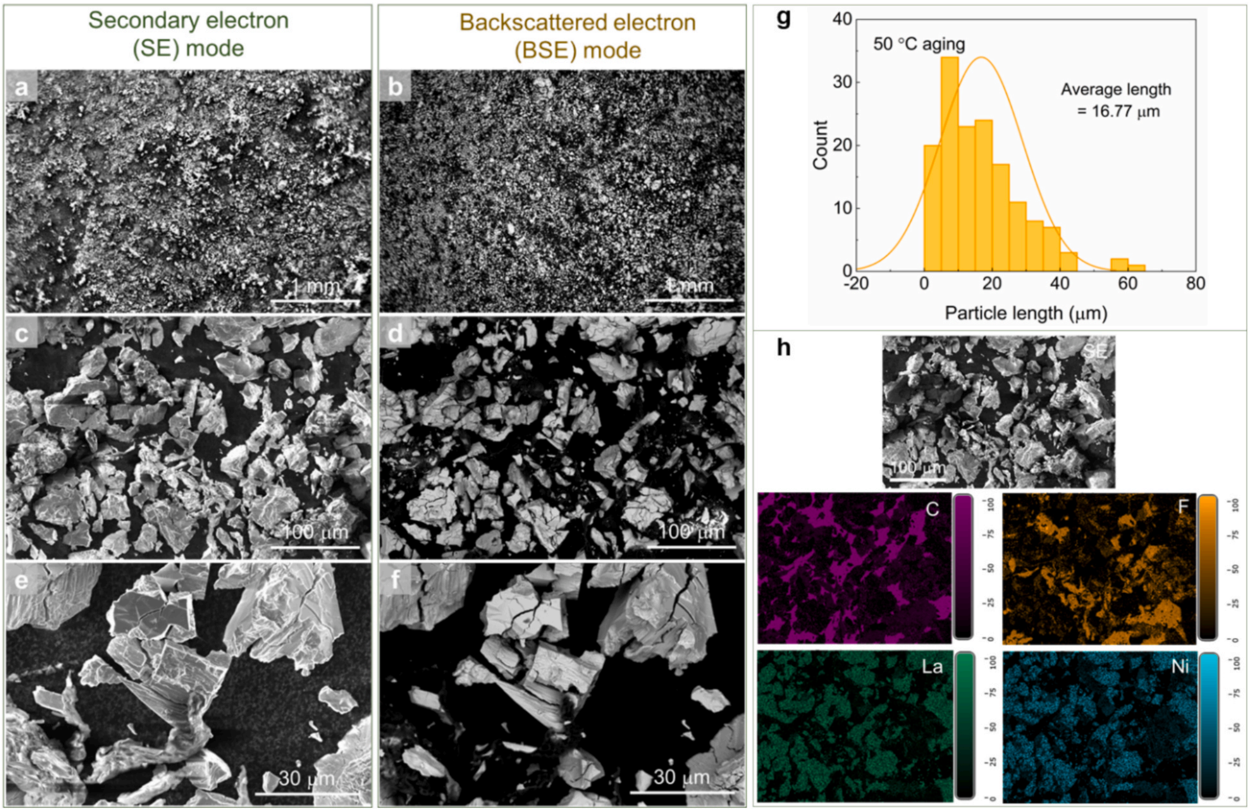

Fig. 9. SEM results of the LaNi$_5$ material aging at 50 °C for 90 days. a, c, e SE images of the 50 °C aged material at different magnifications. **b, d, f** The corresponding BSE images of the 50 °C aged material at different magnifications. **g** The particle size distribution obtained by SEM. **h** The SE image of the 50 °C aged material and corresponding EDS mapping for the elements of C, F, La, and Ni, respectively.

temperatures. For instance, only 0.43 and 0.77 wt% hydrogen can be released when dehydrogenating for 30 min at 20 and 30 °C, respectively. Whereas, the material can desorb 0.99 wt% hydrogen at 40 and 50 °C. The 130 °C aged sample takes less than 0.8 min to reach 90 % of the total hydrogenation hydrogen content than the other samples, as demonstrated in Fig. 4g. There are no significant differences in the dehydrogenation time between this material and the materials that were aged at 50 and 90 °C. Fig. 4d displays the hydrogenation and dehydrogenation kinetics of the 160 °C aged sample measured at 20, 30, 40 and 50 °C. Consistently with the PCI findings, this material has a hydrogen storage capacity of 0.49 wt%. For all investigated temperatures, the time needed to complete 90 % of the hydrogenation process is under 0.3 min (Fig. 4h). Whereas, for all the investigated temperatures, the time required to achieve 90 % of the dehydrogenation capacity is under 3 min. In particular, at 20 °C, these findings show that the hydrogenation and dehydrogenation rates of the material as well as its achievable hydrogen storage capacity are affected by material aging.

Based on the PCI and kinetic curves, it is clear that the exposures to increasing temperatures and pressures affect the material properties (including hydrogen storage capacity and thermodynamic properties) in a discernible way, thus indicating that the aging effects are indeed sensible. For understanding the reason behind the observed phenomena, in-depth microstructural investigations were carried out via SR-PXD, QENS, SEM-EDS and SAXS techniques in the following.

3.3. *Microstructure evolutions*

To analyze the microstructure evolution of the different specimens, SR-PXD analyses of the samples before and after aging were carried out. The SR-PXD pattern of the as received material (Fig. 5a) indicates that LaNi$_5$ is the main phase in all samples, with no detectable reflections corresponding to other phases such as Ni or La. However, due to the aging process, the intensities for different Bragg reflection peaks were changed. For example, the intensities of the (1–1–1) and (2–2–2) reflections decrease after aging, while the intensities of the (200) and (002) reflections show clear increments after aging. Note that the intensities of the peaks were normalized to ensure that the comparison is meaningful. Fig. 5b illustrates the lattice constants of the samples. LaNi$_5$ crystallizes in the hexagonal structure of space group P6/mmm. The lattice constants a and c obtained for the as received sample are 5.0242 ± 1.9 × 10^{-4} Å and 3.9822 ± 8.5 × 10^{-4} Å, respectively and the c/a ratio is equal to 0.793. The c value for samples aged at 50, 90, and 130 °C exhibits a clear increasing trend. The a values decrease after aging except for the sample aged at 160 °C. Additionally, a noticeable increase in the c/a ratio is observed. These changes reveal that there may be some residual compressive stresses on the a-axis and some residual tensile stresses on the c-axis after the aging studies.

Understanding the evolution of the lattice strain is apparently essential for revealing the aging mechanism. The lattice strain (ε) for each lattice plane was calculated by the following equation:

$$\varepsilon_{hkl} = \frac{d_{hkl} - d_{hkl,0}}{d_{hkl,0}} \tag{4}$$

where d_{hkl} is the d-spacing of the hkl lattice plane, and $d_{hkl,0}$ is the d-spacing of the hkl lattice plane of the reference samples, in this case, the as received LaNi$_5$. As can be seen in Fig. 5c, the lattice strain depends on the crystallographic planes, indicating the materials' behavior during aging is anisotropic. The (001) plane shows the largest lattice strain, which means that this plane has the lowest elastic stiffness by assuming the stress for each material is identical. Also notice that the lattice strain on most of the planes increases after aging. The changes of FWHM were also calculated, see Fig. 5d. The FWHM increases after aging for all planes, especially for the (200). Note that particle size decrement and

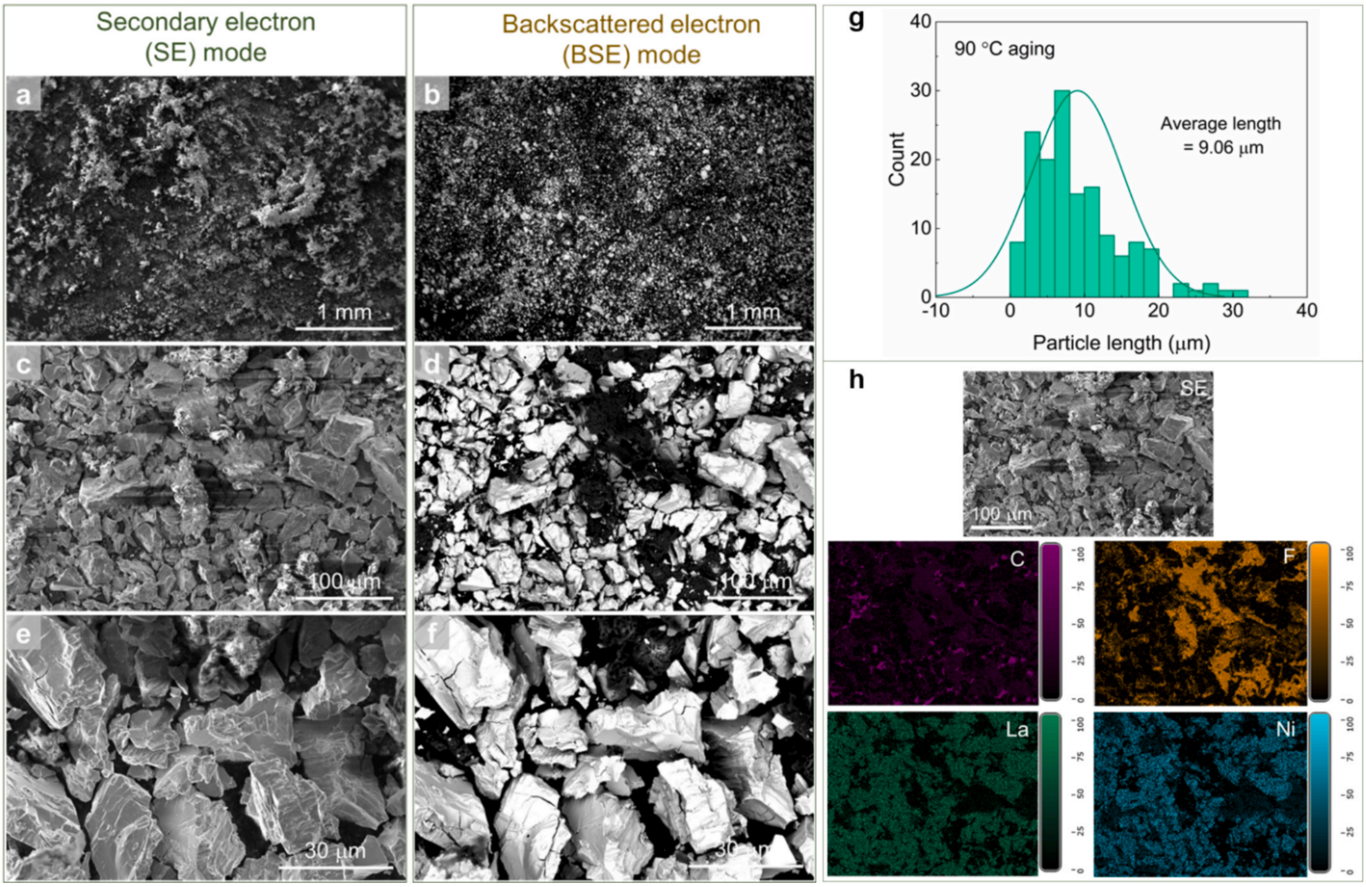

Fig. 10. SEM results of the LaNi$_5$ material aging at 90 °C for 90 days. a, c, e SE images of the 90 °C aged material at different magnifications. **b, d, f** The corresponding BSE images of the 90 °C aged material at different magnifications. **g** The particle size distribution obtained by SEM. **h** The SE image of the 90 °C aged material and corresponding EDS mapping for the elements of C, F, La, and Ni, respectively.

lattice strain increment are potential causes of peak broadening.

To further unveil the reason behind the observed aging phenomena, the parameters related to defects, such as dislocation density (ρ) were analyzed by using the SR-PXD data. Williamson and Hall [12] proposed that the physical line broadening ΔK can be determined by the following equations:

$$\Delta K = \frac{0.9}{D} + \varepsilon K \tag{5.1}$$

$$\Delta K = 2\Delta\theta\frac{\cos\theta}{\lambda} \tag{5.2}$$

$$K = \frac{2\sin\theta}{\lambda} = \frac{q}{2\pi} \tag{5.3}$$

where D is the crystallite size, $\Delta\theta$ is the FWHM in the SR-PXD patterns, λ is the wavelength and ε is the lattice strain. The relation between lattice strain and dislocation density can be written as:

$$\rho = B\left(\frac{\varepsilon}{b}\right)^2 \tag{6}$$

where b is the length of the Burgers vector, and B is a uniform parameter related to the elastic modulus and dislocation configuration of the material.

However, if we consider that the elastic module for the lattice is anisotropic, dislocations on a specific crystal plane cause different distortions on different crystal planes. Therefore, the value of B is influenced by the anisotropic behavior of the material. Ungár and Borbély [13] considered the distortion caused by dislocations on different crystal planes, and pointed out to use the average contrast factor (C) to modify the K parameter, which is called the modified Williamson-Hall method:

$$\Delta K = \frac{0.9}{d} + \left(\frac{\pi M^2 b^2}{2}\right)^{\frac{1}{2}} \rho^{\frac{1}{2}} K C^{\frac{1}{2}} + O\left(K^2 C\right) \tag{7}$$

where $O(K^2C)$ is a high-order term of $KC^{1/2}$ and is usually ignored. M is a parameter that depends on the effective outer cut-out radius (R_e) of dislocations and the dislocation density ($M = R_e\rho^{\frac{1}{2}}$ [14], of which $\ln\frac{R_e}{b} = 2\pi$). The value of C is affected by the elastic constants, dislocation type and crystal plane index. For the hexagonal structure, C is given by the following equation [15,16]:

$$C = C_{hk,0}\left(1 + q_1 H_1^2 + q_2 H_2^2\right) \tag{8}$$

of which $H_1^2 = \frac{\left[h^2+k^2+(h+k)^2\right]l^2}{\left[h^2+k^2+(h+k)^2+\frac{3}{2}\left(\frac{a}{c}\right)^2 l^2\right]^2}$ and $H_2^2 = \frac{l^4}{\left[h^2+k^2+(h+k)^2+\frac{3}{2}\left(\frac{a}{c}\right)^2 l^2\right]^2}$.

Here, the h, k and l are the Miller indices corresponding to each diffraction peak. The C values in this case were calculated by using the ANIZC [17] software.

Note that the instrumental broadening also contributes to the profile line broadening of the samples, therefore, it has to be deducted before calculating the ρ values. Here we used the following function to get the peak broadening from the samples:

$$\Delta K_{sample} = \left(\Delta K_{mesaure}^2 - \Delta K_{instrument}^2\right)^{\frac{1}{2}} \tag{9}$$

where $\Delta K_{measure}$ and $\Delta K_{instrument}$ are the peak broadening values from the

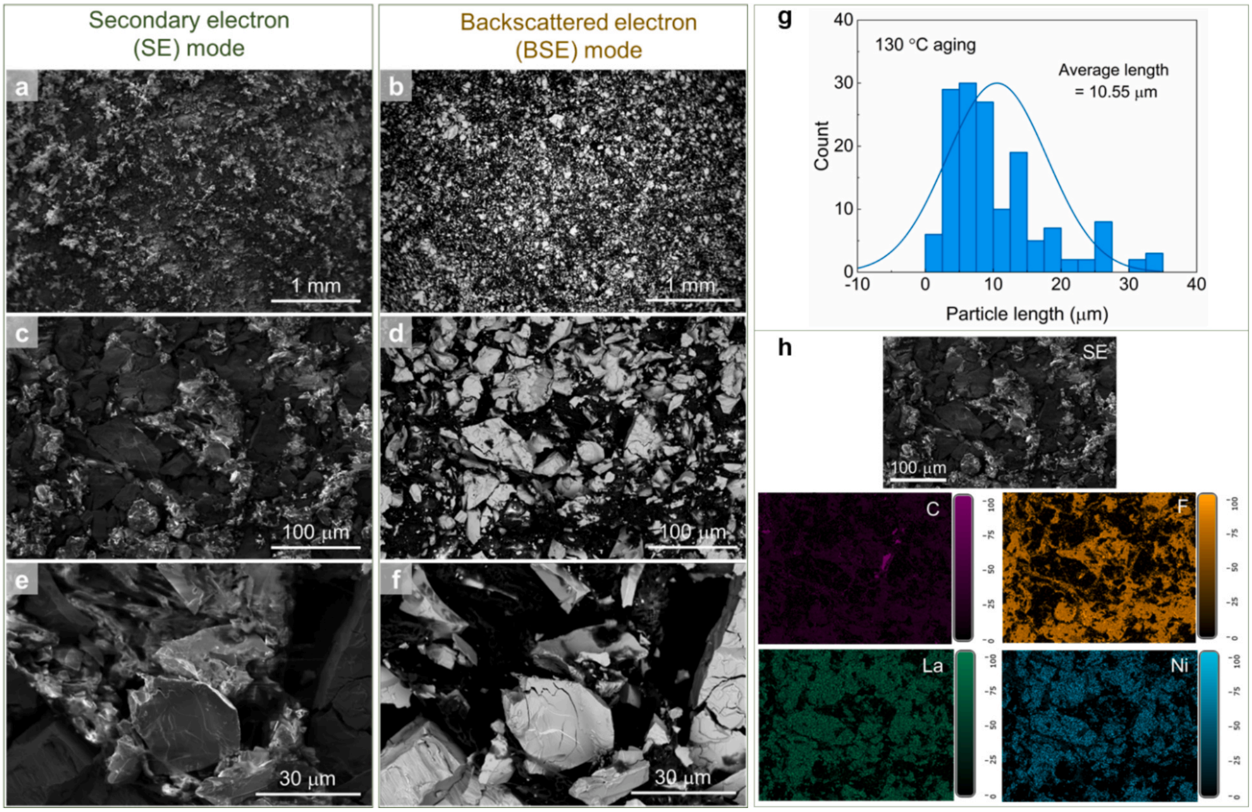

Fig. 11. SEM results of the $LaNi_5$ material aging at 130 °C for 90 days. a, c, e SE images of the 130 °C aged material at different magnifications. **b, d, f** The corresponding BSE images of the 130 °C aged material at different magnifications. **g** The particle size distribution obtained by SEM. **h** The SE image of the 130 °C aged material and corresponding EDS mapping for the elements of C, F, La, and Ni, respectively.

measurement and instrument, respectively. The instrumental broadening was obtained from the standard LaB_6 material.

By applying linear fitting of the ΔK versus $KC^{1/2}$ (Fig. 6a), the value of ρ can be obtained from the slope. The obtained dislocation densities for each sample are shown in Fig. 6b. If we assume that all the dislocations in the samples are edge dislocations, we can see that for the as received $LaNi_5$, the dislocation density is 6.72×10^{14} m^{-2}. After aging, the dislocation density increases gradually with temperature, where the dislocation density is around 16.77×10^{14} m^{-2} for the sample aged at 160 °C, which is more than 2 times of that for the as received material. If we would assume that all the dislocations are screw dislocations, the dislocation densities are smaller than those for edge dislocation, but with aging at different temperatures, the same trend is observed. The results indicate that aging has a strong influence on the dislocation density and thus affects the materials' properties.

The QENS spectra of the as received and 160 °C aged samples are shown in Fig. 7. These measured spectra were fitted according to **Eq. (3)**. The fit comprises two components: an elastic contribution represented by the Delta function, $\delta(\omega)$, and a quasi-elastic broadening component described by the Lorentzian function $L(Q,\omega)$. The spectra of both samples appear similar, suggesting a comparable chemical environment across the samples. Furthermore, the fit results show no quasi-elastic broadening, indicating the absence of observable motion in these samples. The results are in good agreement with the SR-PXD data, indicating that there is no hydrogen-related phase presented in all aged samples even for the $LaNi_5$ aged at the highest temperature (160 °C) for 90 days.

Scanning electron microscopy with SEM-EDS was used to study the material particles' morphology and particle size distribution. Additionally, the mapping of elemental distribution was carried out. SEM images of the as received material are shown in Fig. 8. Both the secondary electron (SE) and backscattered electron (BSE) images (Fig. 8a-f) show that the size distribution of metal hydride particles is not homogeneous, while the metal hydride particles are embedded well in Teflon. For each sample, 200 particles were selected, and their size was measured using ImageJ software. This data was subsequently analyzed and fitted to a Gaussian distribution model, yielding the average particle size. The average particle length of the as received material was calculated to be 28.96 μm, see Fig. 8g. From the EDS mappings for the elements of C, F, La, and Ni (Fig. 8h), it appears clear that the $LaNi_5$ metal hydride is embedded in a polymeric matrix. One particle of the metal hydride was selected to check the elemental composition, see **Fig. S1**. The quantitative results are shown in **Table S1**. Although the atomic ratios between La and Ni are not exactly 5:1, they are still in the range of 4:1 to 5:1, confirming that the investigated phase is $LaNi_5$.

Images from SEM of the material after 90 days of aging at 50 °C indicate that the size of metal hydride particles is smaller than that of the as received material. Cracks are visible in some particles (Fig. 9a-f). As clearly shown in Fig. 9g, the average particle size decreases to 16.77 μ m in comparison to Fig. 8g. It is evident from the EDS mappings (Fig. 9h) that the $LaNi_5$ metal hydride is embedded in the Teflon. Next, the elemental compositions of a single metal hydride particle in three sites were determined, as shown in **Fig. S2**, where **Table S2** summarizes the relevant EDS quantitative results. Since La and Ni appear always in combination and with the ratio close to 1 to 5, the main phase after aging at 50 °C is still $LaNi_5$.

For the material aged at 90 °C for 90 days, SE and BSE images in Fig. 10a-f illustrate that the size of metal hydride particles decreases, and several micro-cracks are present in some particles. The average particle size further decreases to 9.06 μ m, as displayed in Fig. 10g. From the EDS mappings for the elements of C, F, La, and Ni in Fig. 10h, It is evident that the distribution of Ni and La share an abundance of similarities and consistency. The elemental compositions (see **Table S3**) of some selected spots in **Fig. S3** also prove that the precipitation of LaH

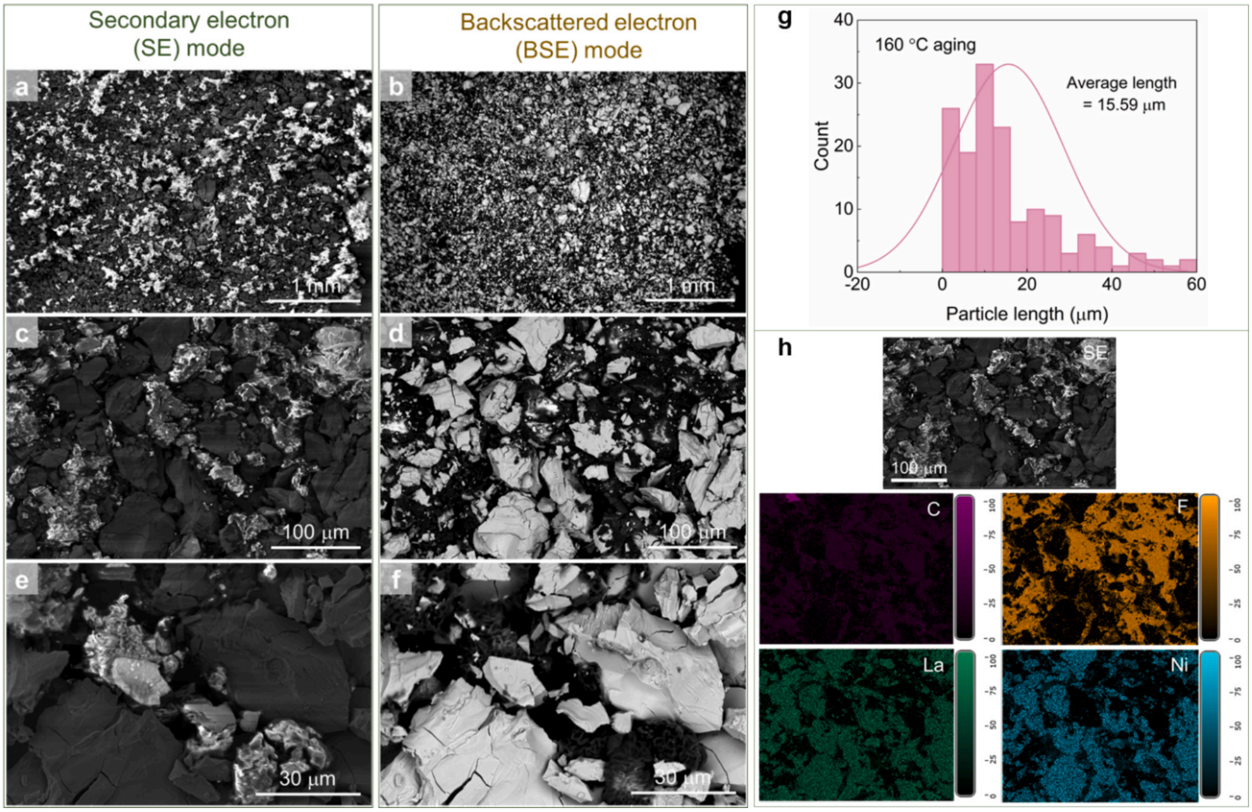

Fig. 12. SEM results of the LaNi$_5$ material aging at 160 °C for 90 days. a, c, e SE images of the 160 °C aged material at different magnifications. **b, d, f** The corresponding BSE images of the 160 °C aged material at different magnifications. **g** The particle size distribution obtained by SEM. **h** The SE image of the 160 °C aged material and corresponding EDS mapping for the elements of C, F, La, and Ni, respectively.

and Ni did not occur.

The SEM analyses of the material aged at 130 (Fig. 11) and 160 °C (Fig. 12), similar to the samples aged at 50 and 90 °C, present sizes of metal hydride particles smaller than that of the as received materials. Several cracks in the particles are observed in this case too. Note that the average particle sizes for 130 °C aged and 160 °C aged samples are 10.55 (Fig. 11g) and 15.59 μ m (see Fig. 12g), respectively. The EDS mappings for the elements of C, F, La, and Ni in Fig. 11h and Fig. 12h demonstrate that the distributions of these elements are homogeneous. The EDS findings for several selected spots for the 130 °C aged (**Fig. S4** and **Table S4**) and 160 °C aged (**Fig. S5** and **Table S5**) samples indicate that the overall specimen consists of LaNi$_5$. In summary, micro-cracks were detected in the aged samples, but not in the as received material. The lattice expansion induced by hydrogenation during aging can be the predominant factor for this [18]. Upon hydrogenation, the cell volume expansion of LaNi$_5$ can reach values from 20 % up to 27 % [19]. Other factors such as temperature and hydrogen pressure can minorly contribute to the lattice expansion. As can be seen in Fig. 10f-11f, the fracture in the alloy powders is transverse, implying a hydrogenation-induced micro-crack mechanism, which is in good agreement with the results reported by Kastrissios et al. [20]. It is crucial to note that since the hydrogenation does not occur in all locations at the same time, the stresses caused by the mismatch between the metal and metal hydride matrixes will then cause cracks to form and propagate [20]. The analyses indicate that within the resolution of SEM, the average particle size of the LaNi$_5$ after aging gets smaller than the as received material, although it does not linearly depend on the aging temperature. It is important to point out that the observed changes are merely a few micrometers, despite SEM analyses revealing that the average particle sizes for samples aged at 130 and 160 °C (10.55 and 15.59 μm, respectively) exceed those of samples aged at 90 °C (9.06 μm). The selection of only 200 particles for quantitative analysis may have contributed to the observed discrepancies, as the particle size distribution within the sample was not homogeneous. In addition, no phase segregation of LaNi$_5$ was observed after aging.

As these results clearly show, the aging process of the samples has been accompanied by structural changes at the microscopic level. To further detail these changes, the material microstructural features in the nanoscale were investigated via the SXAS technique. The experimental data and the fitted curves for all samples are shown in Fig. 13a-e, and the corresponding size distributions are shown in Fig. 13**f-k.** For the fitting of the scattering curves, a spherical geometry of the particle distribution was assumed, as a first approximation. Due to the system's complexity, the particle size distributions were analyzed using SASfit software, employing a Log-Normal distribution fitting, which yielded results that closely matched the experimental data (Fig. 13). From the size distribution of the samples, we can see a clear trend in the decrement of particle sizes with respect to increasing of aging temperatures. The average particle sizes, in the observed *q*-range of the SAXS setup, for the as received LaNi$_5$ are roughly 116.6 nm, whereas for those aged at 50, 90, 130 and 160 °C are about 82.3, 58, 54.9 and 38 nm, respectively. The particle sizes are significantly reduced with aging, which further supports the microscopic SEM findings at the nanoscopic scales. Therefore, in general, it can be stated that the aging process of the LaNi$_5$ leads to an overall structural refinement of the system.

3.4. Aging mechanisms

In this section, the aim is to acquire information on the material behavior after a lifetime of 12 years. Therefore, a lifetime model should be obtained from the accelerated aging tests. Two essential parameters were considered for expressing the hydrogen storage properties of the materials. One parameter is the hydrogen storage capacity, reflecting the hydrogen content in the metal hydrides, while the other is the

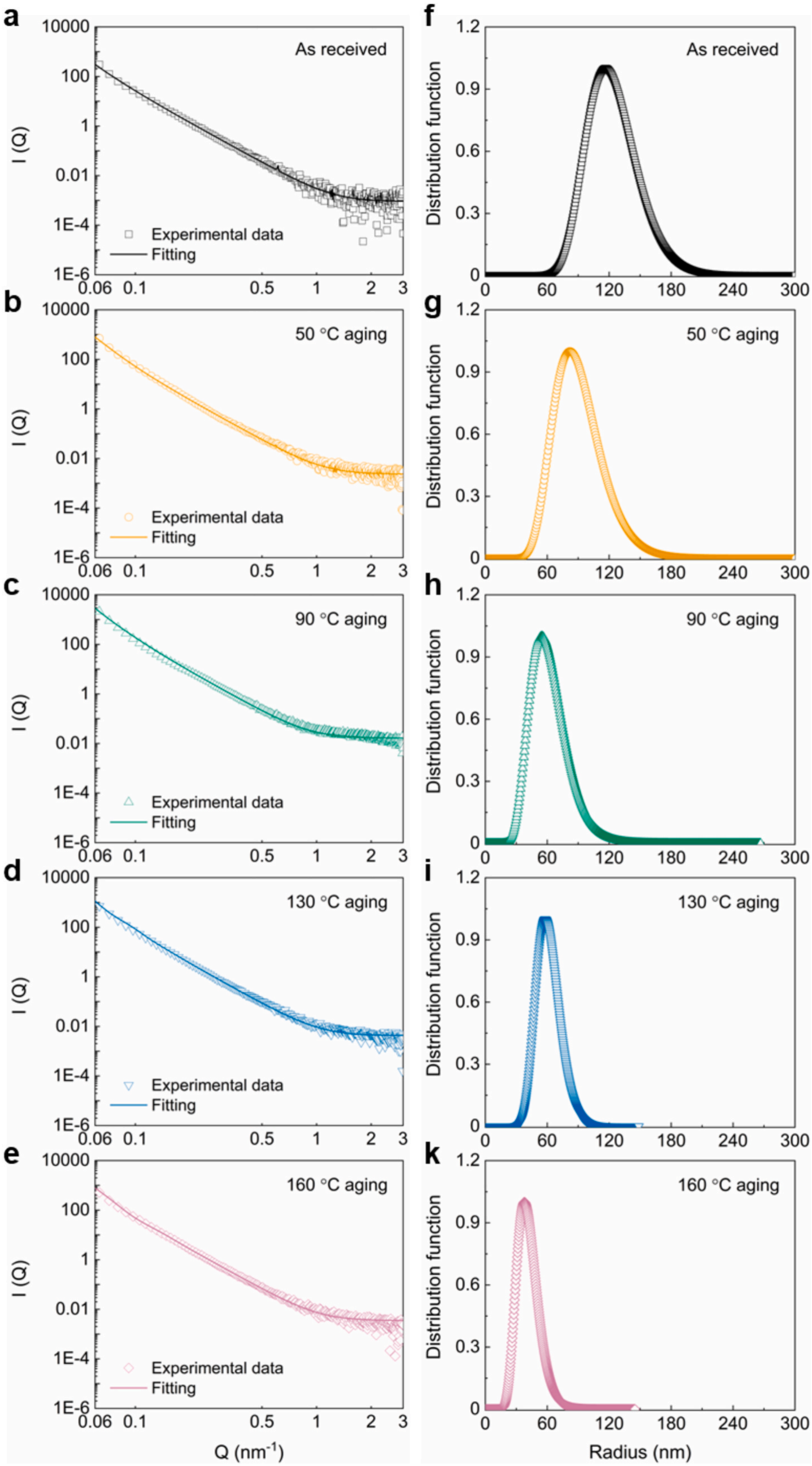

Fig. 13. Small-angle X-ray scattering (SAXS) data of the as received material as well as the materials aging for 90 days at 50, 90, 130 and 160 °C. a-e Experimental and fitting data of as received material as well as the materials aging for 90 days at 50, 90, 130 and 160 °C. **f-k** Size distributions of the particles obtained from **a-e** for the as received material as well as the materials aging for 90 days at 50, 90, 130 and 160 °C.

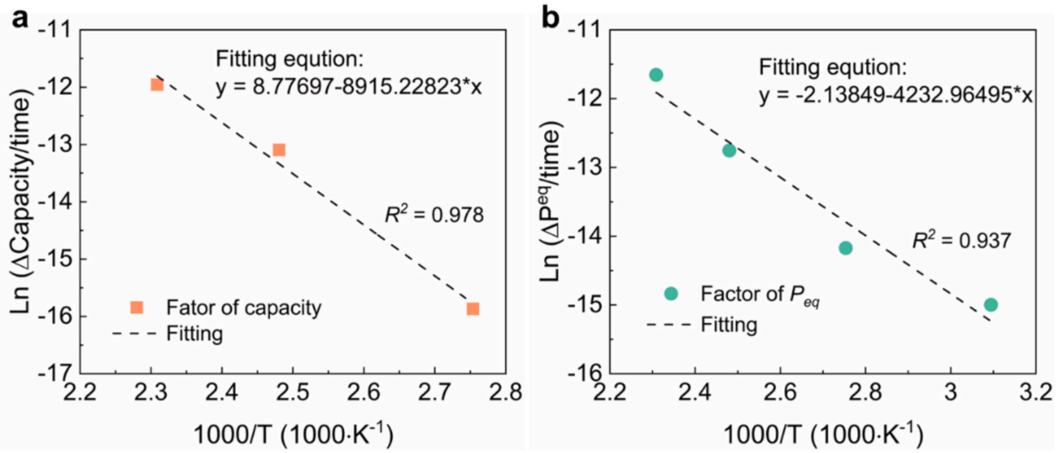

Fig. 14. **a** Temperature dependency of the aging factor of hydrogen storage capacity over temperature for tests performed for 90 days together with a linear regression. **b** Temperature dependency of the aging factor of dehydrogenation equilibrium pressure at 30 °C over temperature for tests performed for 90 days together with a linear regression.

equilibrium dehydrogenation pressure, which reflects the thermodynamic characteristics of the metal hydrides. First, the plateau capacity was taken as one factor and the data aging for 90 days for fitting was utilized. In this case, $\alpha = \Delta\text{Capacity}/t$, where ΔCapacity is the capacity change compared to the original capacity, and t is the aging time. Fig. 14a shows the relationship between the aging factor of hydrogen storage capacity and the temperature. The linear regression shows that the fitted equation is $\ln(\Delta\text{Capacity}/t) = 8.77697 - 8915.22823/T$. Therefore, based on this equation, we can calculate that after 12 years, if operating at 30 °C, ΔCapacity is around 0.152 % of the original plateau capacity (0.0016 wt%). In the case of operating at 50 °C for 12 years, ΔCapacity is around 0.415 % of the original plateau capacity (0.0044 wt %).

Secondly, we took the equilibrium pressure for dehydrogenation at 30 °C as one factor and used the data of aging for 90 days for fitting. Fig. 14b exhibits the relationship between the aging factor of equilibrium pressure for hydrogenation and the temperature. In this case, $\alpha = \Delta P_{eq}/t$, where ΔP_{eq} is the equilibrium pressure change compared to the original value, and t is the aging time. The linear regression shows that the fitted equation is $\ln(\Delta P_{eq}/t) = -2.13849 - 4232.96495/T$. Based on this equation, we can calculate that after 12 years, if operating at 30 °C, ΔP_{eq} for 30 °C might decrease around 38.47 % of the original equilibrium pressure. If operating at 50 °C for 12 years, ΔP_{eq} for 30 °C might decrease around 91.28 % of the original equilibrium pressure.

From the microstructure characterizations, it is clear that no phase segregation was observed after aging. This is quite interesting since, according to some earlier research [21], cycling studies indicate that phase segregation to LaH and Ni may be the source of the $LaNi_5$ deterioration. Therefore, after careful study, it can be concluded that the $LaNi_5$ hydrogen storage properties' degradation is not related to the formation of new phases, which gives a new perspective on the regeneration/reactivation of $LaNi_5$. From one point of view, we noticed that after aging, the dislocation density increases and particle size decreases, indicating that the degradation may mainly come from the nanostructuring of the materials. The hydrogen pressure stresses the $LaNi_5$ lattice, which causes the lattice strain to rise. This raises the lattice parameter of c, which in turn impacts the concentration of defects, primarily dislocation density. It can be observed that the particle size also reduces with aging because, after strain accumulates up to a certain level, some cracks begin to form in order to release the strain. Even though it isn't included in this study, the findings will make it easier for the degraded materials to regenerate or reactivate by applying heat treatments to the samples to relieve any remaining strain inside the lattice. From another point of view, despite thermodynamic expectations, the precipitation of LaH and Ni during aging was not observed in this work. However, previous studies have demonstrated that the precipitation of LaH and Ni occurs upon thermal or pressure cycling [22–26]. This finding can be related to the fact that static conditions were applied in this study (the material was continuously in the hydrogenated state). Whereas in the works reported in the literature, by extensive cycling, the material has been subjected to continuous expansive and contractive forces that locally might have generated stresses, which led to the overcoming of the precipitation barrier of LaH and Ni. One possible explanation for the degradation of the storage capacity is that during aging, the overall hydrogen sites may be lost due to samples' continued cracking, formation of grain boundaries and localized amorphization.

4. Conclusions

A series of tests were performed on $LaNi_5$ materials and the results obtained from the accelerated aging tests indicate that after 12 years, the materials' capacity degradation lies between around 0.152 % (operating at 30 °C) and 0.415 % (operating at 50 °C) of the original capacity. After 12 years, the plateau pressure for dehydrogenation at 30 °C will decrease from around 38.47 % (operating at 30 °C) to 91.28 % (operating at 50 °C). No phase segregation was observed after aging but only the dislocation density increases and particle size decreases, indicating that the degradation may mainly come from the nanostructuring of the materials. This work provides some insights into the designing strategies for predicting the degradation of the metal hydride's hydrogen storage properties and bodes well for providing practical guidance and methods to prolong the metal hydride life for the manufacturers. This work sheds light on how to establish approaches for predicting degradation of the metal hydrides' hydrogen storage properties. It also paves the way for offering manufacturers useful guidance and strategies to prolong the metal hydrides' life.

CRediT authorship contribution statement

Yuanyuan Shang: Writing – original draft, Visualization, Validation, Methodology, Investigation, Data curation, Conceptualization. **Ting Chen:** Writing – review & editing, Investigation. **Fahim Karimi:** Writing – review & editing, Investigation. **Thi Thu Le:** Writing – review & editing, Data curation. **Jürgen Markmann:** Writing – review & editing, Resources. **Jan Peter Embs:** Visualization, Resources. **Benjamin Klusemann:** Writing – review & editing, Resources. **Thomas Klassen:** Supervision, Project administration, Funding acquisition. **Claudio Pistidda:** Writing – review & editing, Supervision, Resources,

Project administration, Funding acquisition.

Declaration of competing interest

The authors declare that they have no known competing financial interests or personal relationships that could have appeared to influence the work reported in this paper.

Acknowledgement

This research was partially funded by dtec.bw – Digitalization and Technology Research Center of Bundeswehr which we gratefully acknowledge. We acknowledge DESY (Hamburg, Germany), a member of the Helmholtz Association HGF, for the provision of experimental facilities. Parts of this research were carried out at PETRA III and we would like to thank Dr. Alexander Schökel for assistance in using photon beamline P02.1. Beamtime was allocated for proposal I-20231121.

Appendix A. Supplementary data

Supplementary data to this article can be found online at https://doi.org/10.1016/j.cej.2025.161682.

Data availability

Data will be made available on request.

References

[1] R.G. Ross, Aerospace coolers: a 50-year quest for long-life cryogenic cooling in space, Cryogenic Engineering, Springer (2007) 225-284, https://doi.org/10.1007/0-387-46896-X_11.

[2] H.S. Cao, B.Q. Liu, L.X. Qin, Sorption cryogenic cooling: Fundamentals, progress, and outlook, Appl. Therm. Eng. 213 (2022) 118680, https://doi.org/10.1016/j.applthermaleng.2022.118680.

[3] R.C. Bowman, Metal Hydride Compressors with Gas-Gap Heat Switches: Concept, Development, Testing, and Space Flight Operation for the Planck Sorption Cryocoolers, Inorganics 7 (12) (2019) 139, https://doi.org/10.3390/inorganics7120139.

[4] R. Levenduski, R. Scarlotti, Joule-Thomson cryocooler for space applications, Cryogenics 36 (1996) 859–866, https://doi.org/10.1016/0011-2275(96)00049-5.

[5] K. Malleswararao, P. Dutta, M.S. Srinivasa, Applications of metal hydride based thermal systems: A review, Appl. Therm. Eng. 215 (2022) 118816, https://doi.org/10.1016/j.applthermaleng.2022.118816.

[6] M.V. Lototskyy, V.A. Yartys, B.G. Pollet, R.C. Bowman, Metal hydride hydrogen compressors: A review, Int. J. Hydrogen Energ. 39 (2014) 5818–5851, https://doi.org/10.1016/j.ijhydene.2014.01.158.

[7] J.N. Yang, A. Zavabeti, Y.L. Guo, Z. Yu, L. Dehdari, J.N. Guo, C. Wu, D.Q. Wang, J. M. Goh, P.Y. Xiao, G.K. Li, Recovery of low-concentration hydrogen using alloy LaNi5 based pressure swing adsorption, Chem. Eng. J. 493 (2024) 152395, https://doi.org/10.1016/j.cej.2024.152395.

[8] D. Pearson, R. Bowman, M. Prina, P. Wilson, The Planck sorption cooler: Using metal hydrides to produce 20 K, J. Alloy Compd. 446 (2007) 718–722, https://doi.org/10.1016/j.jallcom.2006.11.202.

[9] J. Wise, K.T. Gillen, R.L. Clough, An Ultrasensitive Technique for Testing the Arrhenius Extrapolation Assumption for Thermally Aged Elastomers, Polym. Degrad. Stabil. 49 (1995) 403–418, https://doi.org/10.1016/0141-3910(95)00137-B.

[10] A.P. Hammersley, FIT2D: an introduction and overview, European synchrotron radiation facility internal report, ESRF97HA02T 68 (1997) 58.

[11] I. Bressler, J. Kohlbrecher, A.F. Thunemann, SASfit: a tool for small-angle scattering data analysis using a library of analytical expressions, J. Appl. Crystallogr. 48 (2015) 1587–1598, https://doi.org/10.1107/S1600576715016544.

[12] G.K. Williamson, W.H. Hall, X-Ray Line Broadening from Filed Aluminium and Wolfram, Acta Metall. Mater. 1 (1953) 22–31, https://doi.org/10.1016/0001-6160(53)90006-6.

[13] T. Ungar, A. Borbely, The effect of dislocation contrast on x-ray line broadening: A new approach to line profile analysis, Appl. Phys. Lett. 69 (1996) 3173–3175, https://doi.org/10.1063/1.117951.

[14] O.B. Pedersen, The Flow-Stress of Copper, Acta Metall. Mater. 35 (1987) 2567–2581, https://doi.org/10.1016/0001-6160(87)90154-4.

[15] T. Ungár, G. Ribárik, L. Balogh, R. Thomas, O. Koc, M. Preuss, C.P. Race, P. Frankel, Fractional densities and character of dislocations in different slip modes from powder diffraction patterns, J. Nucl. Mater. 589 (2024) 154828, https://doi.org/10.1016/j.jnucmat.2023.154828.

[16] I.C. Dragomir, T. Ungár, Contrast factors of dislocations in the hexagonal crystal system, J. Appl. Crystallogr. 35 (2002) 556–564, https://doi.org/10.1107/S0021889802009536.

[17] A. Borbély, J. Dragomir-Cernatescu, G. Ribárik, T. Ungár, Computer program ANIZC for the calculation of diffraction contrast factors of dislocations in elastically anisotropic cubic, hexagonal and trigonal crystals, J. Appl. Crystallogr. 36 (2003) 160–162, https://doi.org/10.1107/S0021889802021581.

[18] E. Alvares, K. Sellschopp, B. Wang, S.Y. Kang, T. Klassen, B.C. Wood, T.W. Heo, P. Jerabek, C. Pistidda, Multiscale modeling of metal-hydride interphases-quantification of decoupled chemo-mechanical energies, Npj Comput Mater 10 (2024) 249, https://doi.org/10.1038/s41524-024-01424-1.

[19] C. Briki, P. de Rango, S. Belkhiria, M.H. Dhaou, A. Jemni, Measurements of expansion of LaNi5 compacted powder during hydrogen absorption/desorption cycles and their influences on the reactor wall, Int J Hydrogen Energ 44 (2019) 13647–13654, https://doi.org/10.1016/j.ijhydene.2019.04.010.

[20] T. Kastrissios, E. Kisi, S. Myhra, Hydrogen activation of LaNi5: Implications of fracture mechanisms on hydriding properties, J. Mater. Sci. 30 (1995) 4973–4979, https://doi.org/10.1007/BF01154511.

[21] F.T. Zohra, C.J. Webb, K.E. Lamb, E.M. Gray, Degradation of metal hydrides in hydrogen-based thermodynamic machines: A review, Int. J. Hydrogen Energ. 64 (2024) 417–438, https://doi.org/10.1016/j.ijhydene.2024.03.228.

[22] S. Ono, K. Nomura, E. Akiba, H. Uruno, Phase Transformations of the LaNi5-H2 System, J. Less-Common Met. 113 (1985) 113–117, https://doi.org/10.1016/0022-5088(85)90153-5.

[23] T. Matsumoto, A. Matsushita, A New Intermediate Hydride in the LaNi5-H2 System Studies by Insitu X-Ray-Diffractometry, J. Less-Common Met. 123 (1986) 135–144, https://doi.org/10.1016/0022-5088(86)90123-2.

[24] J.E. Bonnet, P. Dantzer, H. Dexpert, J.M. Esteva, R. Karnatak, Modifications near the Surface Owing to Hydrogen Cycling of the Intermetallics LaNi5 and LaNi5-XAlx, J. Less-Common Met. 130 (1987) 491–495, https://doi.org/10.1016/0022-5088(87)90146-9.

[25] E.M. Gray, T.P. Blach, C.E. Buckley, Stability of the hydrogen absorption and desorption plateaux in LaNi-H -: Part 5: H capacity, J. Alloy Compd. 293 (1999) 57–61, https://doi.org/10.1016/S0925-8388(99)00301-1.

[26] M.L. Post, J.J. Murray, Calorimetric Identification of a Eutectoid Phase-Separation in the Lani5-H-2 System at T Almost-Equal-to 350-K, J. Solid State Chem. 86 (1990) 160–163, https://doi.org/10.1016/0022-4596(90)90130-P.